

2009-01-01

High-Temperature Phase Transitions In RbH_2PO_4

Heber Jair Martinez

University of Texas at El Paso, heber_jair@hotmail.com

Follow this and additional works at: https://digitalcommons.utep.edu/open_etd



Part of the [Condensed Matter Physics Commons](#)

Recommended Citation

Martinez, Heber Jair, "High-Temperature Phase Transitions In RbH_2PO_4 " (2009). *Open Access Theses & Dissertations*. 306.
https://digitalcommons.utep.edu/open_etd/306

This is brought to you for free and open access by DigitalCommons@UTEP. It has been accepted for inclusion in Open Access Theses & Dissertations by an authorized administrator of DigitalCommons@UTEP. For more information, please contact lweber@utep.edu.

HIGH-TEMPERATURE PHASE TRANSITIONS IN RbH_2PO_4

HEBER MARTINEZ

Department of Physics

APPROVED:

Cristian E. Botez, Ph.D., Chair

Russell R. Chianelli, Ph.D.

Marian-Mihai Manciu, Ph.D.

Patricia D. Witherspoon, Ph.D.
Dean of the Graduate School.

Copyright ©

by

Heber Martinez

2009

HIGH-TEMPERATURE PHASE TRANSITIONS IN RbH_2PO_4

by

HEBER MARTINEZ

THESIS

Presented to the Faculty of the Graduate School of

The University of Texas at El Paso

in Partial Fulfillment

of the Requirements

for the Degree of

MASTER OF SCIENCE

Department of Physics

THE UNIVERSITY OF TEXAS AT EL PASO

May 2009

Acknowledgements

I am very grateful to my advisor Dr. Cristian Botez for his support and patience during the course of this research project. His knowledge, advising and insight about the research topics and instrumentation used in this project have been invaluable to me and have contributed enormously in every part of this project. It has been a privilege to work with him.

I would also like to thank Drs. Russell Chianelli and Marian-Mihai Manciu for serving on my thesis committee. I thank Dr. Chianelli of the Materials Research and Technology Institute at UTEP for his collaboration in the sample preparation process of this project.

Thanks to Dr. Ron Tackett for his great help inside the laboratory and with different matters in the writing process of this thesis.

Big thanks to Dr. Jorge Lopez and Mrs. Terry Weber for their help with innumerable administration and immigration troubles that I ran into during my graduate studies. A special thanks goes for Dr. Jorge Lopez for his tutoring in probably all of the masters in physics classes and for his constant advice on random things faced at school.

I would like to thank Dr. Milijana Suskavcevic for her support and mentoring during my first year in the Masters in Physics program.

Thanks to my peers and friends Christian, Enrique, Marco, Sunil, Richard, Mayra, Anthony, Judith, Lala, Eder, Felipe, and Dr. Eric Hagedorn, for sharing with me the intellectual and practical challenges of graduate school as well as sharing many adventures inside and outside of school.

A very special thanks that I cannot express with words goes to my father Manuel Martinez who has been with me every single day during my graduate studies.

Abstract

High Temperature Phase Transitions in RbH_2PO_4

M.S. candidate: Heber Martinez

Advisor: Dr. Cristian E. Botez

Recent studies have shown that the proton conductivity of MH_2PO_4 ($\text{M}=\text{Cs}$, Rb) solid-acids exhibits a sharp, several-order-of-magnitude increase upon heating above a certain temperature threshold [Boysen *et al.*, Chem. Mater. **15**, 727(2003), Boysen *et al.*, Chem. Mater. **16**, 693(2004)]. This so-called superprotonic behavior allows the above-mentioned compounds to function as fuel-cell electrolytes at intermediate temperatures [Boysen *et al.*, Science **303**, 68(2004)], a remarkable application that has attracted much interest. Yet, the crystal structures and microscopic mechanisms responsible for this heating-induced proton conductivity enhancement are not fully understood.

Our group has previously demonstrated [Botez *et al.*, J. Chem. Phys. **127**, 194701(2007)] that the superprotonic behavior in CsH_2PO_4 is due to the transformation of its room-temperature monoclinic ($\text{P } 2_1/\text{m}$) phase into a high-temperature cubic ($\text{P } \text{m } 3 \text{ m}$) polymorph at 237°C . Although a similar jump in the proton conductivity upon heating has been reported for RbH_2PO_4 [Boysen *et al.*, Chem. Mater. **16**, 693(2004)], recent thermal analysis and qualitative X-ray diffraction (XRD) studies [Ortiz *et al.*, J. Phys. Chem. Solids **59**, 1111(1997), J.-H. Park *et al.*, J. Phys. Cond. Mat. **13**, 9411(2001)] have suggested that the room temperature tetragonal ($\text{I } -4 2 \text{ d}$) RbH_2PO_4 phase actually decomposes via dehydration at temperatures as low as 96°C .

Surprisingly, this implies that RbH_2PO_4 's superprotonic behavior cannot be due to a polymorphic phase transition.

In our present studies we attempt to clarify the structural and/or chemical modifications of RbH_2PO_4 upon heating within the 25-250°C temperature range. We use temperature- and time-resolved powder x-ray diffraction (XRD) methods on polycrystalline samples obtained by crushing single RbH_2PO_4 crystals previously prepared by slow evaporation. Our XRD data, collected in the reflectivity geometry over the 1.5-3.5Å d-spacing range, evidence a tetragonal-to-monoclinic transition that occurs within the 90-110°C temperature interval. We indexed the high temperature monoclinic phase to space group $\text{P2}_1/\text{m}$ and lattice parameters $a=7.728\text{\AA}$, $b=6.187\text{\AA}$, $c=4.810\text{\AA}$, and $\beta=109.15^\circ$. We have also carried out Rietveld refinements that conclusively demonstrate that the newly observed monoclinic structure is a RbH_2PO_4 polymorph. These results are significant as they unambiguously establish that prior to any temperature induced chemical changes, RbH_2PO_4 transforms into a stable polymorph, whose crystal structure is *isomorphic to the monoclinic structure* observed in room temperature CsH_2PO_4 . This strongly suggests that the superprotonic behavior in RbH_2PO_4 is triggered by a monoclinic-cubic polymorphic phase transition *similar* to the one observed in CsH_2PO_4 . Unfortunately, our current experiments could not reveal such a transition as, upon further heating to 210°C under ambient pressure and humidity conditions, the monoclinic phase starts dehydrating via the reaction $2\text{RbH}_2\text{PO}_4 = \text{Rb}_2\text{H}_2\text{P}_2\text{O}_7 + 2\text{H}_2\text{O}$. A possible method to avoid dehydration in future experiments involves the heating of samples subjected to high pressures of about 1GPa [Boysen *et al.*, Chem. Mater. **15**, 727(2003), Boysen *et al.*, Chem. Mater. **16**, 693(2004), Botez *et al.*, J. Chem. Phys. **127**, 194701(2007)]

Table of Contents

	Page
Acknowledgements.....	iv
Abstract.....	v
Table of contents.....	vii
List of tables.....	ix
List of figures.....	x
Chapters	
1 Introduction.....	1
1.1 Earth's energy resources	1
1.2 A promise for the future: Fuel cells.....	1
1.2.1 Types of fuel cells and their limitations.....	2
1.2.2 Electrolytes.....	3
1.2.3 Proton conductivity and solid acids.....	4
1.2.4 Phosphoric acids.....	5
2 Theoretical Background.....	10
2.1 Crystal structure.....	11
2.1.1 Lattice.....	11
2.1.2 Basis.....	11
2.1.3 Unit cell.....	12
2.1.4 Crystal symmetry.....	13
2.1.5 Lattice point groups.....	13

	2.1.6	Space groups.....	14
	2.1.7	Crystal systems.....	14
	2.1.8	Miller indices.....	15
	2.2	The Bragg condition.....	16
	2.3	X-ray powder diffraction.....	17
	2.4	Data interpretation.....	18
3		Experimental Procedure.....	21
	3.1	Sample preparation.....	21
	2.1	Apparatus.....	22
	2.2	Methodology.....	23
4		Results and discussion.....	27
5		Summary and conclusions.....	37
		References.....	38
		Curriculum Vita.....	40

List of Tables

	Page
Table 1: Fractional coordinates and thermal parameters of non-hydrogen atoms in RbH_2PO_4	32
Table 2: Comparison between unit cell parameters and PO_4 tetrahedral bond distances and angles in the monoclinic phases of rubidium- and cesium-dihydrogen phosphate.....	33

List of Figures

	page
Figure 1.1: Diagram of a proton exchange membrane (PEM) hydrogen fuel cell.....	2
Figure 2.1: Crystal structure in two dimensions.....	12
Figure 2.2: Lattice parameters.....	13
Figure 2.3: The seven crystal systems.....	15
Figure 2.4: Axes intercepts giving Miller indices (111) on the left structure and (112) on the right structure.....	16
Figure 2.5: Illustration of Bragg's law.....	17
Figure 2.6: Cone shaped reflections from powder diffraction.....	18
Figure 2.7: An x-ray powder diffraction pattern.....	19
Figure 3.1: The synthesis process for RbH_2PO_4	21
Figure 3.2: Mortar and pestle (left). RbH_2PO_4 crystals (right).....	22
Figure 3.3: Siemens D-5000 diffractometer.....	22
Figure 3.4: Diffraction geometry.....	23
Figure 3.5: FULLPROF starting parameters file.....	24
Figure 3.6: Le Bail fit where red dots are XRD data points, black line is Le Bail fit and blue line is difference curve.....	25
Figure 3.7: Cell parameters given by the Le Bail fit.....	26
Figure 4.1: XRD pattern of RbH_2PO_4	28

Figure 4.2: Indexing of RbH_2PO_4 at (a) room temperature: tetragonal

RbH_2PO_4 . (b) high temperature: monoclinic RbH_2PO_429

Figure 4.3: Rietveld fit and 3-D model of monoclinic RbH_2PO_431

Figure 4.4: Le Bail fits for three temperature regions (upper panel).

Temperature dependence of lattice parameters of

RbH_2PO_434

Figure 4.5: Dehydration and partial decomposition of RbH_2PO_4 at high

temperatures.....35

Chapter 1: Introduction

1.1 Earth's energy resources

Expiring fossil fuels, and their impact on the environment has motivated research into alternative fuels as well as more “eco-friendly” methods of energy production. Much of this work has centered on novel energy production methods using devices such as fuel cells and alternative fuel sources such as natural gas, solar power, ethanol, and other renewable non-fossil-fuel sources of energy. The goal of this work revolves around making these alternative fuels and technologies available and affordable to the masses, thus allowing for the replacement of gasoline, diesel and other nonrenewable sources of energy that contribute largely to the Earth's pollution.

1.2 A promise for the future: Fuel cells

Fuel cells are a clean, alternative source of power and some of the most promising devices for the future generation of electricity. Fuel cells take in fuel through the anode side, whereby a catalyst decomposes the fuel into electrons and positive ions, sending the electrons through an outer circuit, while the positive ions are transported through an electrolyte to the cathode. There, an oxidizing agent is combined with the electrons and positive ions to form water, in the case of hydrogen fuel cells, or other substances depending on the type of fuel employed [1]. The hydrogen fuel cell, for example, utilizes hydrogen gas (H_2) as fuel and oxygen (O_2) in the air as the oxidizing agent at the cathode; in these fuel cells, hydrogen is separated into protons and electrons by a catalyst at the anode. Subsequently, the electrons are passed through an outer circuit making an electrical current, and the protons passed through an electrolyte

membrane. Upon arrival at the cathode, the protons and electrons are combined with molecular oxygen by a catalyst to form water and heat as the waste products of the fuel cell. These and other characteristics have paved the way for research into the development and engineering of new and better fuel cells.

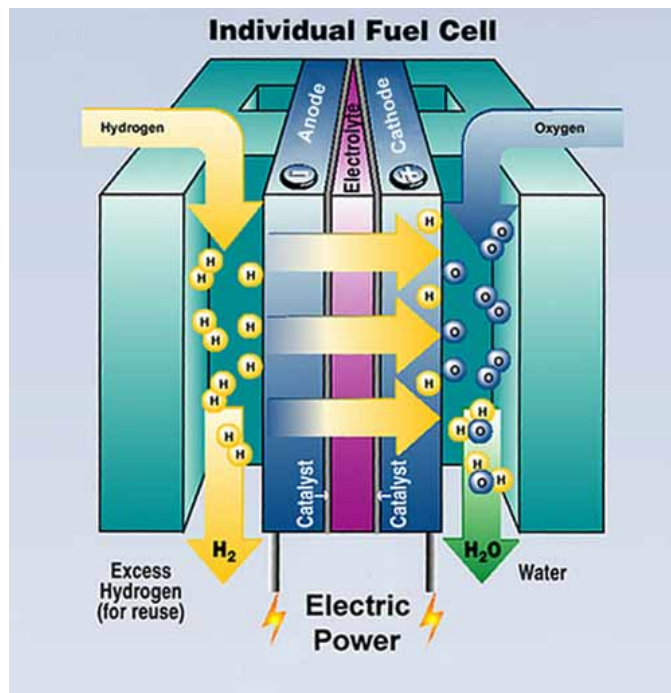


Figure 1.1: Diagram of a proton exchange membrane (PEM) hydrogen fuel cell

1.2.1 Types of fuel cells and their limitations

Research and production of different kinds of fuel cells has been ongoing for several decades. Some types of fuel cells have achieved very good efficiency in terms of power generation, like the molten carbonate fuel cell and the solid oxide fuel cell. Other types of fuel cells have achieved the advantage of compact design and portability such as the proton exchange membrane fuel cell (diagrammed in Figure 1.1) and the direct methanol fuel cell. Unfortunately, many aspects of fuel cells still have a lot of deficiencies. For example, the molten carbonate fuel

cell, which has a very good efficiency because it works at high temperatures and uses its own heat to produce more power, presents the disadvantage of having an unstable electrolyte and limited service life, due in part to the high operating temperatures mentioned. Also, one of the most developed fuel cells so far, the proton exchange membrane fuel cell, has a high production cost due in great part to the expense of the catalyst, which is generally platinum. An alternative solution to this problem is being developed by a research group at Monash University, Melbourne: a cheaper fuel cell made of a new conducting polymer cathode called poly (3, 4-ethylenedioxythiophene) or PEDOT [2]. Another deficiency in fuel cells is that some, like the proton exchange membrane fuel cells, require humidification of the polymer electrolyte membrane (which conduct protons as hydronium) with liquid water to work efficiently, meaning that they can only operate competently at temperatures below 100°C [3]; if the temperature in the fuel cells exceeds this range, the water evaporates and the membrane dries, which causes it to fail in performance. In addition, most fuel cells need pure hydrogen to work best, and production and transportation of hydrogen fuel is expensive due to the safety issues involved with H₂ gas.

These and other aspects of critical importance for the performance of a fuel cell are therefore being studied in order to develop a better understanding of the microscopic processes that occur in each part of the fuel cell. Improved knowledge of these processes will, no doubt, allow for better designs, as well as more efficient and affordable fuel cells.

1.2.2 Electrolytes

One of the most efficient fuel cells in use today is the Proton Exchange Membrane Fuel Cell (PEMFC) [1]. This fuel cell uses hydrogen fuel and oxygen to generate electricity by means of an electrochemical reaction. A vital part of these devices, is the electrolyte membrane. The

electrolyte is responsible for the transportation of protons from the anode to the cathode, where they combine with electrons and oxygen to form water and heat.

From the first fuel cell created in 1839 until today, there have been many electrolytes used. Examples include potassium hydroxide, polymer membranes, humic acids, sodium hydroxide, Nafion[®] (a sulfonated tetrafluorethylene copolymer), and solid-acids [1]. The first fuel cells used materials similar to the ones used today in phosphoric-acid fuel cells, and the later created sulphonated polystyrene ion-exchange membranes. [1]

1.2.3 Proton conductivity and solid acids

Many efforts have been made to improve these electrolytes, and more importantly, develop a better understanding of the chemical and physical nature of the electrolyte's function in a fuel cell: proton conductivity. A material is said to become superprotonic, when its proton conductivity suddenly increases by orders of magnitude upon heating. A special type of fuel cell electrolytes are solid-acids. Some of these materials, such as sulfates and selenates have exhibited these so-called superprotonic transitions at temperatures above 140 °C [4]. In addition, superprotonic solid-acids can conduct protons without the need for water. This remarkable characteristic of sulfates and selenates makes solid-acids an appealing option over polymer electrolytes for operation at temperatures greater than 100°C. Additionally, this makes the idea of portable fuel cells more feasible, since the anhydrous proton transport in this type of electrolyte eliminates the need of having an additional system to maintain the fuel cell under a saturated water vapor environment.

The first successful solid-acid based fuel cell was produced in 2001 by Haile *et. al.*[5]. This fuel cell used a 1.5 mm thick layer of CsHSO₄ as the electrolyte membrane and functioned

in the temperature range from 150-160°C. The fuel cell produced an open-circuit voltage of 1.11V and a current density at short circuit of 44 mA/cm². This sulfate-based solid-acid is stable under oxidizing conditions but loses weight under reducing conditions as it reacts with hydrogen, producing the catalyst poison H₂S. Other sulfate and selenate based electrolytes undergo similar reactions in fuel cells [6]. These catalyst poisons cause the erosion of the anode over time, and decrease the efficiency of the fuel cell. This has motivated research into the properties of phosphate-based solid-acids for use as fuel cell electrolytes.

1.2.4 Phosphoric acids

Researchers have shown that phosphate-based solid-acids have similar high-temperature proton conducting abilities to the above mentioned sulfates and selenates. However, phosphate-based solid-acids do not react with the hydrogen fuel to produce catalyst poisons that can erode the electrodes, thus making phosphate-based solid-acids a more appealing option for fuel cell electrolytes than the previously mentioned sulfates and selenates. Experiments have shown that CsH₂PO₄ (CDP) and RbH₂PO₄ (RDP) exhibit superprotonic behavior when heated above a high temperature threshold [7,8]. A CDP-based fuel cell was shown to operate properly and continuously for over one hundred hours, evidence that CDP can function efficiently as a fuel cell electrolyte [9]. This achievement has generated a great amount of interest from the theoretical and the engineering perspectives; however, it is left to the researchers to unveil the microscopic mechanisms responsible for the sudden increase in the proton conductivity observed in these materials. Studies have shown that the proton conduction mechanisms in these fully-hydrogen-bonded compounds must, in principle, be different from those responsible for the high proton conductivity exhibited by their half-hydrogen-bonded, sulfate-based counterparts (e.g.

CsHSO₄) [10]. Therefore, a different type of proton dynamics must be present in the superprotonic phases of these phosphate-based solid-acids. In order to propose an accurate atomic-level explanation of the proton migration in these materials, a detailed knowledge of the crystal structures and chemical processes present in the materials at all temperatures in the range close to the superprotonic transition is needed.

There has been much debate over the cause of this sudden increase in proton conductivity in CDP and RDP. Is it a chemical modification of the compounds, or is it a change in the structure of the material? One group believes that this superprotonic behavior is due to the decomposition and dehydration of the electrolyte, while another group argues that it is due to a change in the crystal structure of the material. Lee *et. al.*, Ortiz *et. al.*, and Park *et.al.* [11, 12, 13, 14] provide evidence that the superprotonic behavior is due to thermal decomposition and dehydration of the material. Others, like Botez *et. al.*, Brownowska *et. al.*, Baranov *et. al.* and Boysen *et. al.* [15, 16, 17, 7] agree that the enhanced proton conductivity is due to a polymorphic phase transition.

CDP has been shown to undergo a structural phase transition to a high-symmetry cubic phase at a temperature of approximately 230°C, a temperature commensurate with the onset of superprotonic behavior [7]. Impedance measurements on CDP reveal that, at the transition temperature, the proton conductivity of the sample changes suddenly from $1.2 \times 10^{-5} \Omega^{-1}cm^{-1}$ to $9.0 \times 10^{-3} \Omega^{-1}cm^{-1}$ [7, 8]. Botez *et. al.* conclude that CDP undergoes a structural transition from a monoclinic (P2₁/m) phase, to a dynamically-disordered cubic (Pm3m) phase at the same temperature as the superprotonic transition [15]. Botez *et. al.* and Boysen *et. al.* have performed synchrotron x-ray diffraction experiments under high pressure (~1 GPa) to prevent dehydration in the sample, and discovered that the superprotonic transition in the sample still occurs, even in

the absence of dehydration [7, 15]. They have proved this technique to be useful in solving this debate and have suggested that the technique will be useful in analyzing other phosphate-based solid-acids' superprotonic/structural transitions. These studies have conclusively demonstrated that the superprotonic transition is associated with the change in the crystal structure. Moreover, neutron spectroscopy studies performed on CDP evidence that the characteristics of the high-temperature CDP phase (e.g. its high symmetry, and the six-fold dynamically disordered PO₄ tetrahedra) have an important role in the enhancement of the proton conductivity [18].

It is the above stated reasons that motivate the study of a material similar to CDP, namely RbH₂PO₄ (RDP). RDP also exhibits superprotonic behavior at high temperatures and the question looms as to whether or not this characteristic is due to a structural phase transition similar to the monoclinic to cubic phase transition observed in CDP. There are, however, differences between these two similar compounds which need to be addressed and explained first. For example, RDP has a tetragonal (I-42d) structure at room temperature, different from the monoclinic phase of CDP observed at the same temperature. Tetragonal RDP undergoes a first transformation at a temperature within the 90°C – 130°C interval, considerably below its superprotonic increase temperature (327°C) [8]. Previous research has evidenced this intermediate-temperature transformation of tetragonal RDP; however, the vast majority of these studies were based on thermal analysis methods, which are not capable of providing detailed information about the crystal structure of the samples under investigation. One study used x-ray diffraction experiments on RDP samples kept at 110°C and found a different diffraction pattern than the room-temperature XRD patterns previously recorded [19]. However, according to the authors of Ref. 19, due to heating induced twinning and crystal fragmentation, structure determination was not possible. The authors conclude that the modification in the RDP structure

at 110°C was most likely isomorphic to KD_2PO_4 , i.e. monoclinic $\text{P}2_1/\text{m}$ ($a=7.37\text{\AA}$, $b=14.73\text{\AA}$, $c=7.17\text{\AA}$, and $\beta=92^\circ$).

In another XRD experiment performed by Ortiz *et. al.*, new diffraction peaks were observed for RDP samples previously kept at 150°C, in addition to the peaks associated with the room-temperature tetragonal phase [12]. These new 2θ peak positions do not correspond to the monoclinic RDP structure mentioned in reference [19] or in any other monoclinic structure. Instead, the peaks corresponded to the 2θ positions in the x-ray diffraction pattern of the double salt $2\text{RbH}_2\text{PO}_4 \cdot \text{Rb}_2\text{H}_2\text{P}_2\text{O}_7$. Following these findings, Ortiz *et. al.* conclude that the change in the structure of RDP heated to near 100°C is not a tetragonal to monoclinic phase transition, but rather a chemical decomposition/polymerization and dehydration given by the reaction: $4\text{RbH}_2\text{PO}_4 \rightarrow 2\text{RbH}_2\text{PO}_4 \cdot \text{Rb}_2\text{H}_2\text{P}_2\text{O}_7 + \text{H}_2\text{O}$. An experiment performed by Park *et. al.* [20, 21], in agreement with Ortiz *et. al.*, found, by means of optical microscopy, thermal analysis and impedance spectroscopy measurements that the transformation of RDP at 96°C is indeed due to a chemical decomposition/polymerization given by the above reaction. Moreover, Park proposes a model to explain the superprotonic behavior of phosphate-based solid acids. This model implies that the rapid proton migration is due to the fast breaking and reforming of hydrogen bonds triggered by the dehydration and chemical decomposition of the material. If Ortiz and Park's propositions are correct, then the nature behind RDP's superprotonic behavior is fundamentally different than from that of the chemically similar material CDP determined by Boysen and Botez [7, 15], namely a high-temperature monoclinic to cubic phase transition. It thus becomes important to address this issue, as such a fundamental difference is unlikely to occur.

We performed experiments on polycrystalline RDP aimed at finding its precise crystal structure when heated over a range of temperatures from 30 °C - 200 °C using laboratory powder

x-ray diffraction as well as synchrotron x-ray diffraction. This research is ultimately intended to establish a clear understanding of the superprotonic behavior in phosphate-based solid-acid electrolytes in order to allow for the engineering of better electrolytes based on the proton conduction mechanism present in these superprotonic solid-acids.

Chapter 2: Theoretical Background

In June 8, 1912, a paper entitled “*Interference effects with Rontgen rays*” was submitted to the Bavarian Academy of Sciences in Munich, Germany. In this paper, two important studies were presented. In the first, Laue discusses a basic theory of x-ray diffraction by a periodic array of atoms; and in the second, Friedrich and Knipping report on the first experiments made on x-ray diffraction by crystals. In 1913, Bragg reported on the determination of crystal structures by x-ray diffraction analysis. He determined the structures of KCl, NaCl, KBr and KI. [22]. These studies demonstrated that x-rays are waves, as they can be diffracted from crystalline materials, thus proving that crystals are in fact periodic arrays of atoms [23]. X-ray diffraction has since been used as a powerful technique for the analysis of crystal structures and is the preferred method of analysis for this study.

In this study, the aim is to determine whether the material RbH_2PO_4 (RDP) enters a superprotonic phase at an elevated temperature or if the material changes its nature, *i. e.* decomposes and dehydrates into a different substance with a different crystal structure. Due to the results found by Botez *et. al.*[15] on a similar compound, CsH_2PO_4 (CDP), we expect RDP to undergo a transition to a superprotonic state accompanied by a change in its crystal structure in a similar short temperature interval.

To gain knowledge about the nature of the crystal in discussion we use a technique effective in determining the properties of a crystal: namely x-ray powder diffraction.

2.1 Crystal structure

In the ideal case, a crystal is formed by the repetition of identical structures in three-dimensions. Thus, the crystal structure of a material can be completely described by specifying a lattice, a basis, and the symmetry operations that carry the crystal structure into itself.

2.1.1 Lattice

A lattice can be understood to be a mathematical tool used to describe the position of points on which we attach atoms or groups of atoms. We can describe a lattice by defining three fundamental translation vectors: \mathbf{a} , \mathbf{b} , \mathbf{c} . Consider a point described by the equation

$$\mathbf{r}' = \mathbf{r} + u\mathbf{a} + v\mathbf{b} + w\mathbf{c} . \quad (2.1)$$

In the above equation, the set of points \mathbf{r}' for all integers u, v, w , defines a lattice when the atomic arrangement looks the same when viewed from any point \mathbf{r} as when viewed from any point \mathbf{r}' .

2.1.2 Basis

A lattice is only an imaginary set of points periodically arranged in space. The atoms make the mass in a crystal. To describe the position of the atoms in a crystal we need to specify a basis.

The basis consists of the set of coordinates that describe the positions of the atom or atoms attached to a lattice point: (x_i, y_i, z_i) measured from a lattice point. The lattice together with the basis forms the crystal structure as shown in Figure 2.1.

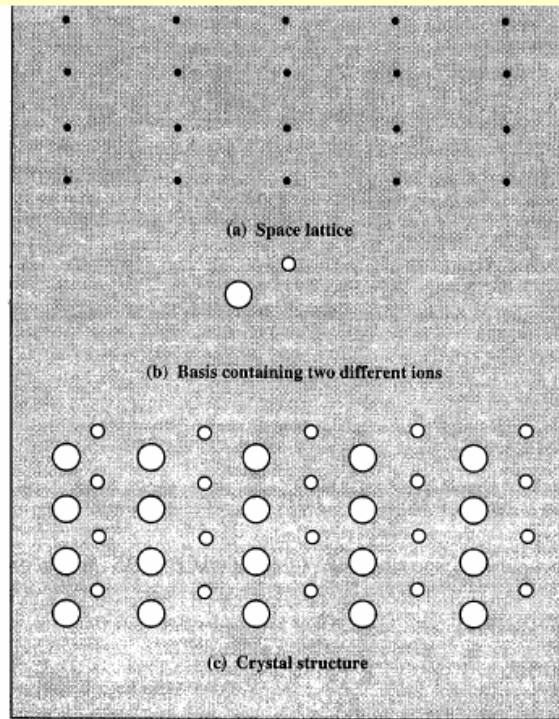


Figure 2.1: Crystal structure in two dimensions

2.1.3 Unit cell

Consecutive lattice points can be thought of as forming microscopic boxes. These boxes are called unit cells and they fill up the space of the lattice. There are many ways to specify a unit cell. For each crystal structure there is a conventional unit cell, which is used to display the full symmetry of the crystal. However, the conventional unit cell may not always be the smallest unit cell that can be stacked to fill the entire lattice space. The smallest unit cell possible is called the primitive unit cell. The primitive unit cell does not always display the full symmetry of the crystal, while the conventional unit cell does. The unit cell has dimensions that depend on the magnitude of the fundamental translation vectors **a**, **b**, **c** and on the angles between these vectors. These dimensions are called the lattice parameters: a , b , c , α , β , γ .

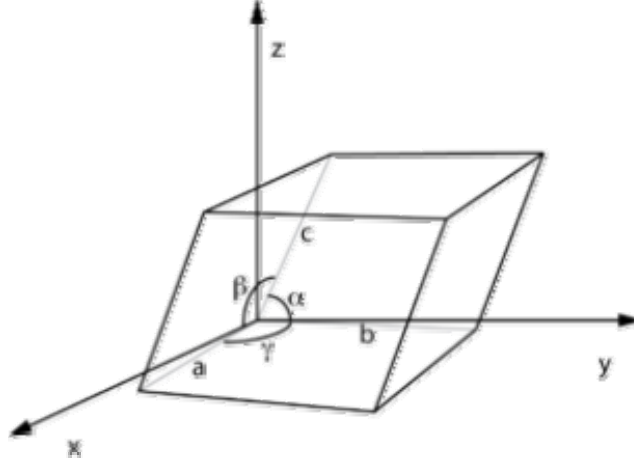


Figure 2.2: Lattice parameters

2.1.4 Crystal symmetry

We know that by stacking unit cells on top of each other and beside each other, we can fill the entire three-dimensional space of the lattice. As mentioned in Kittel [23], this can be done by means of a lattice translation operation: the displacement of a crystal parallel to itself by a crystal translation vector

$$\mathbf{T} = u\mathbf{a} + v\mathbf{b} + w\mathbf{c}, \quad (2.2)$$

where the vector \mathbf{T} connects any two lattice points.

2.1.5 Lattice point groups

According to Kittel [23], we can also perform various symmetry operations to make the crystal lattice be carried onto itself. One of the symmetry operations is rotation about axes passing thorough lattice points. There are only five angles for these rotations which are permissible: 2π , $2\pi/2$, $2\pi/3$, $2\pi/4$ and $2\pi/6$. Another type of operations in a point group are mirror

reflections about a plane through a lattice point. There is also a symmetry operation called an inversion operation, which consists of a rotation by π followed by reflection about a plane that is normal to the rotation axis.

A lattice point group is defined as the collection of the symmetry operations which, when applied about a lattice point, leave the lattice invariant [23]. There are only 32 different point groups allowed by crystalline solids [24].

The requirement that a lattice be invariant under one of the 32 point groups leads to symmetrically specialized types of lattices. These are the Bravais lattices of which there are only 14.

2.1.6 Space groups

As described by Patterson in “Solid State Physics”, associating bases of atoms with the 14 Bravais lattices gives a total of 230 three-dimensional periodic patterns [24]. This means that there are 230 space groups and 230 possible crystal symmetries. These space groups are the combination of the point group operations and the translational symmetry operations of the crystal structure, in addition to screw operations (rotate a point around an axis while translating parallel to the axis), and glide operations (a point through a plane while translating it parallel to the plane). The full symmetry of the crystal structure is contained in the space group.

2.1.7 Crystal systems

The 14 Bravais lattices can be classified in seven systems according to the way in which the lattice parameters a , b , c , α , β , γ , are related. These systems can be classified in seven types of unit cells: triclinic, monoclinic, orthorhombic, tetragonal, cubic, trigonal, and hexagonal.

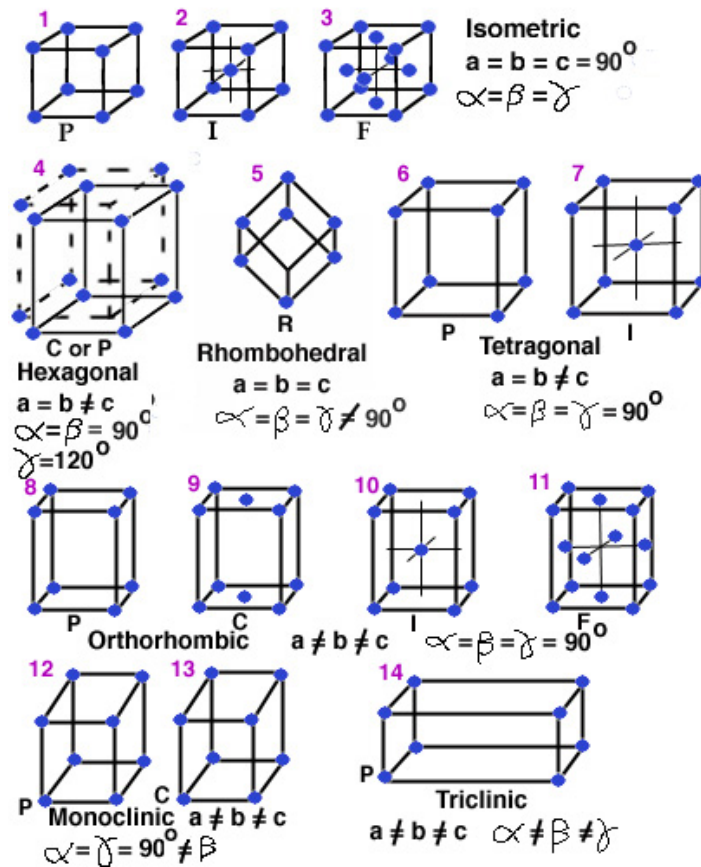


Figure 2.3: The seven crystal systems

2.1.8 Miller indices

The Miller indices (hkl) can be used to describe a plane of atoms, a set of planes of atoms, or a direction in a Bravais lattice. To describe a plane, it is necessary to find the intercepts of the plane on the three axes defined by the fundamental translation vectors **a**, **b**, **c**. Then, take the reciprocal of the three numbers and divide by the greatest common divisor. The resulting three integers are called the Miller indices: (hkl). The set of planes parallel to (hkl) is denoted as {hkl}. [hkl] denotes the direction of a vector normal to the plane (hkl) and <hkl> denotes the set of vectors parallel to [hkl].

Another way to find the Miller indices involves using the reciprocal lattice. Let $\mathbf{d}, \mathbf{e}, \mathbf{f}$, be the reciprocal lattice vectors, then the vector

$$h\mathbf{d} + k\mathbf{e} + l\mathbf{f} \quad (2.3)$$

is normal to the plane (hkl) in the basis of the primitive reciprocal lattice vectors. The constants h, k, l , need to be found by dividing them by their greatest common divisor and making them integers. This means that the Miller indices give us a plane in the real space and a vector normal to the planes of atoms in the reciprocal lattice. A negative integer is represented as a bar above the integer. A plane that does not intercept an axis, has a zero as the Miller index pertaining to that axis.

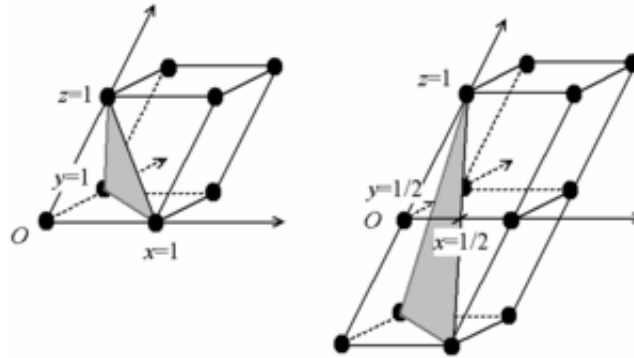


Figure 2.4: Axes intercepts giving Miller indices (111) on the left structure and (112) on the right structure

2.2 The Bragg condition

Suppose two different electromagnetic waves of the same wavelength λ reflect at the same angle θ from two consecutive planes (hkl) of atoms separated by a distance d in a crystal. If both waves are in phase after they reflect, then they interfere constructively and the amplitude of the new wave is doubled. The condition for the waves to be in phase is that they need to travel

the same distance or the difference in distance traveled ($2d\sin\theta$) needs to be an integer multiple of the wavelength λ . This is known as the Bragg condition and is illustrated by Figure 2.5.

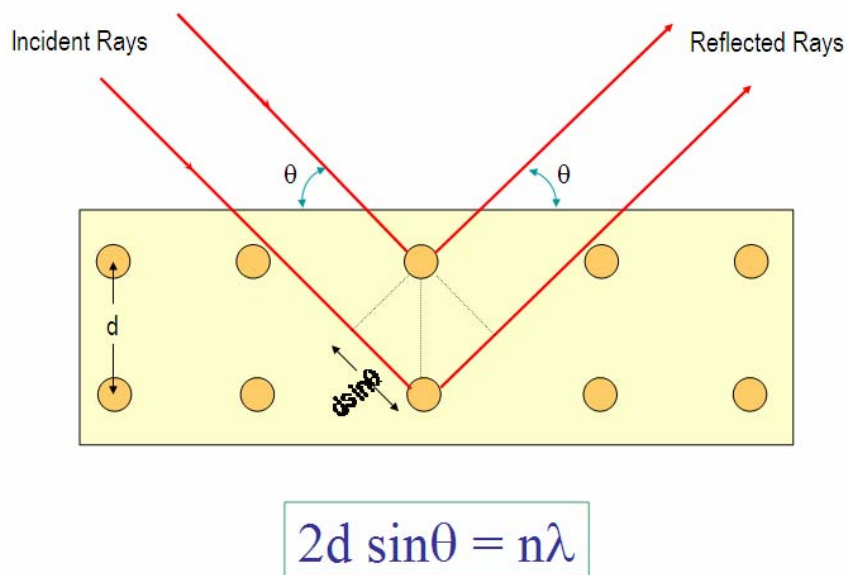


Figure 2.5: Illustration of Bragg's law

2.3 X-ray powder diffraction

Due to the previous observation of a phase change in CDP corresponding to the onset of superprotonic behavior, a study of RDP is warranted to determine if a similar phase transition occurs at a temperature commensurate with the onset of superprotonic behavior in this material. We used powder diffraction because single RDP crystals are not stable (they crack, twin, etc.) at high temperatures that are required to see the phase transitions or chemical modifications in the material.

In x-ray powder diffraction, the crystal being studied is ground into a fine powder, formed by tiny crystals usually measuring ~ 1 micrometer and it is placed in a monochromatic beam of x-rays. Since the crystals in the powder sample are oriented in all possible directions, there will be some planes of atoms in the crystals which will be at the right angles, according to

Bragg's Law, to produce cohesive interference of x-rays. These diffracted x-rays, will produce shapes of cones (Figure 2.6), with high intensity at the angles where the different planes of atoms cause the cohesive interference of x-rays. This pattern gives us the characteristic fingerprint of the material.

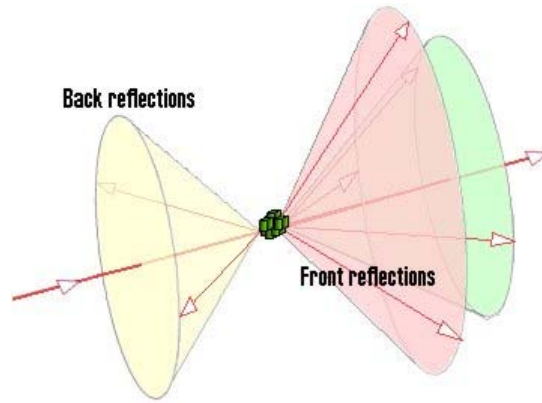


Figure 2.6: Cone shaped reflections from powder diffraction

2.4 Data interpretation

The cone shaped reflections from powder diffraction can be counted and transformed into an intensity versus angle plot to give a clearer picture of the diffraction pattern (Figure 2.7). Computer software is used to count the photons and produce the intensity versus angle graph. This way, we can identify angles with high intensity reflections as peaks in the diffraction pattern. These angles are the Bragg angles θ . Each peak is also related to a plane distance d for a certain $\{hkl\}$ by Bragg's law:

$$\lambda = 2d_{hkl} \sin \theta_{hkl} \quad (2.4)$$

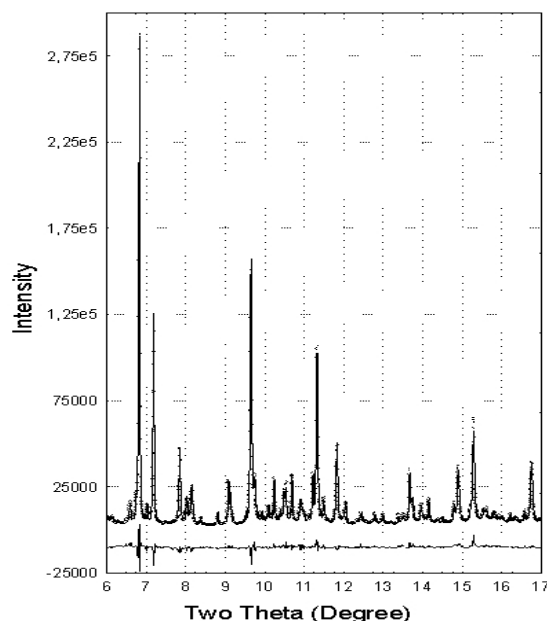


Figure 2.7: An x-ray powder diffraction pattern

Once the data is collected, it needs to be indexed, which involves assigning Miller indices to each peak. This is done by computing the Bragg angles of the diffraction pattern and comparing them to the Bragg angles expected from a certain crystal system.

Bragg angles are related to the Miller indices and to the lattice cell parameters. In the indexing process, one considers Bragg's law and the plane spacing equation for a certain crystal system. The process is aimed at finding the (hkl) and lattice parameters that satisfy the equations for each peak. When the crystal system of the sample is known, indexing is significantly easier for high symmetry systems and more tedious for low symmetry systems.

The $\sin^2 \theta$ terms used in the indexing process for the higher-symmetry systems are the following:

Cubic:

$$\sin^2 \theta_{hkl} = \frac{\lambda^2}{4a^2} (h^2 + k^2 + l^2) \quad (2.5)$$

Tetragonal:

$$\sin^2 \theta_{hkl} = \frac{\lambda^2}{4a^2} (h^2 + k^2) + \frac{\lambda^2}{4c^2} l^2 \quad (2.6)$$

Hexagonal:

$$\sin^2 \theta_{hkl} = \frac{\lambda^2}{3a^2} (h^2 + hk + k^2) + \frac{\lambda^2}{4c^2} l^2 \quad (2.7)$$

Orthorhombic:

$$\sin^2 \theta_{hkl} = \frac{\lambda^2}{4a^2} h^2 + \frac{\lambda^2}{4b^2} k^2 + \frac{\lambda^2}{4c^2} l^2 \quad (2.8)$$

For the other crystal systems, the equations are more complicated, contain more parameters, such as the angles of the unit cell α , β , γ , and the indexing process is very difficult, and is usually done by computer software. This is called autoindexing.

When the powder diffraction pattern does not show peaks expected in a crystal structure, this may be due to systematic absences. Systematic absences give us information about the centering of the unit cell. For example, an I-centered cell shows peaks where $h+k+l$ gives an even number; an F-centered cell shows peaks where hkl are either all even or all odd integers. Also, other systematic absences give us information about the screw axes and glide planes. Altogether, these systematic absences can help us determine the space group of the crystal. The indexing process is complete when all the peaks are indexed.

Chapter 3: Experimental procedure

3.1 Sample preparation

RbH_2PO_4 crystals were synthesized by a vapor diffusion method. The process consisted in mixing rubidium carbonate (Rb_2CO_3) with phosphoric acid (H_3PO_4) below the solubility level. The mixture is then placed in a small beaker and the small beaker is placed inside of a large beaker containing methanol (Figure 3.1). The large beaker was closed with a lid. The system was left at room temperature for approximately two weeks. The RbH_2PO_4 crystals were formed when the methanol vapors mixed with the Rb_2CO_3 and H_3PO_4 solution and caused it to precipitate slowly. This slow process of vapor diffusion produces better crystals than by using a faster method, for example, gel diffusion.

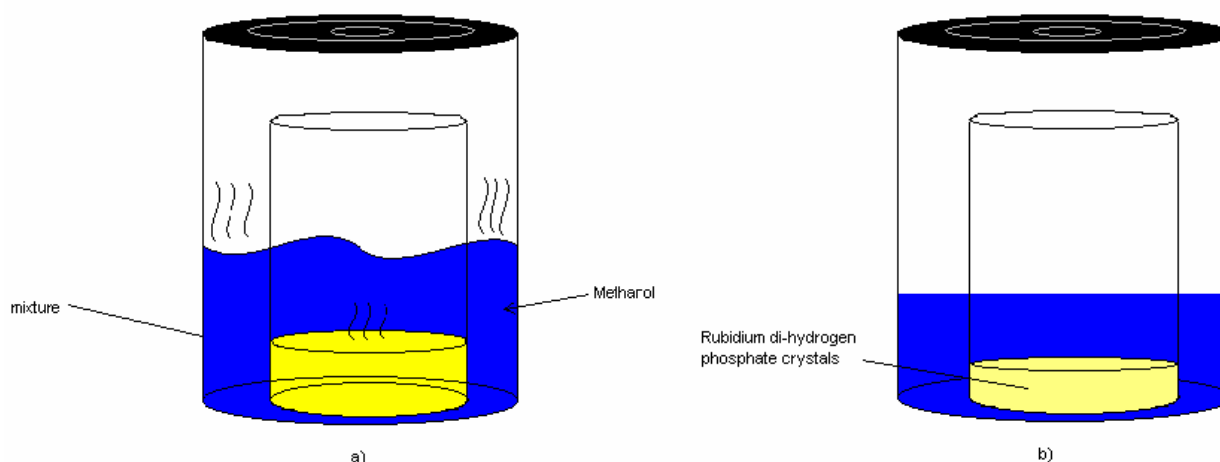


Figure 3.1: The synthesis process for RbH_2PO_4

The crystals were ground mechanically in a mortar and pestle (Figure 3.2) into a fine powder and placed in a sample holder of the x-ray diffractometer.



Figure 3.2: Mortar and pestle (left). RbH_2PO_4 crystals (right).

3.2 Apparatus

The Siemens D5000 x-ray diffractometer (Figure 3.3) was used for the ambient-pressure measurements. The diffractometer has a source of Cu K_α x-rays of wavelength $\lambda = 1.5418 \text{ \AA}$. Any K_β radiation coming from the x-ray tube is removed from the beam by a nickel filter in order to produce a more monochromatic beam of x-rays.



Figure 3.3: Siemens D-5000 diffractometer

The diffractometer has a large diameter goniometer (600 mm) and it can move both its x-rays source and the detector within an angular range from 20° to 60° (Figure 3.4). A Paar

HTK high-temperature chamber that can be used to vary the temperature from room temperature to 1000°C during the XRD data collection was used.

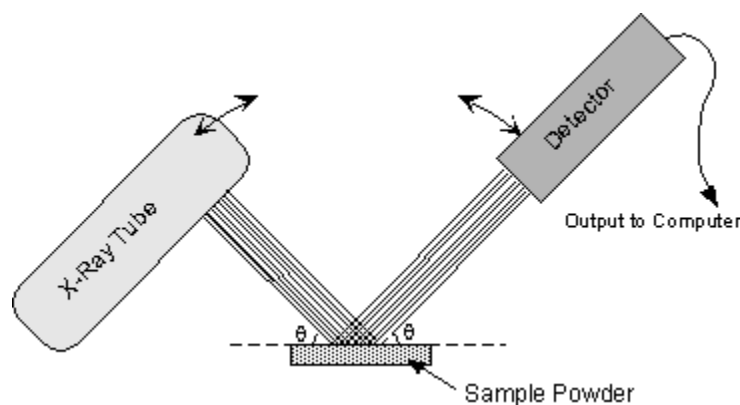


Figure 3.4: Diffraction geometry

3.3 Methodology

In order to run the diffractometer properly, a few key steps need to be performed. First, a steady flow of a gas consisting in 90% argon and 10% methane is flowed through the scintillation counter detector. Second, a steady flow of water at 17° C is ran through the x-ray tube's refrigeration system in order to prevent the x-ray tube from overheating. Thirdly, the detector's manual controls are turned on and a voltage is set at the appropriate level, approx. 3.6 kV. The x-ray tube's voltage is then turned on to no more than 30 kV and its current to no more than 10 mA. Then, after making sure the detector is working properly, the x-ray source's voltage is turned down to 20 kV and its current to 5 mA. subsequently, the experiment is controlled by computer software called Job Measurement. The sample is mounted in place and the door is closed. Using Job Measurement, we input the time intervals and angles at which we want the diffractometer to take measurements. This is done by using a parameter file, created previously. After reading instructions from the file, the system starts taking measurements.

The detector was set to measure scattered x-rays at angles 2θ from 20° to 60° . The total measurement time for each XRD pattern is approximately 30 minutes.

The diffraction pattern was analyzed using a peak fitting software called FULLPROF. This program is used to perform Le Bail analysis. In a Le Bail fit, the unit cell parameters, the reflection intensities, and the peak profile parameters are iteratively adjusted to give the best agreement with the data. The software lets the user choose the parameters to be varied. Then, it makes the best fit possible by varying the lattice parameters in controlled cycles (Figure 3.5).

```

template - Notepad
File Edit Format View Help
COMM Tetragonal RDP
! Current global Chi2 (Bragg contrib.) = 519.6
! Files => DAT-file: rbh2po4_rt, PCR-file: rbh2po4_rt
! Job Npr Nph Nba Nex Nsc Nor Dum Iwg Ilo Ias Res Ste Nre Cry Unl Cor Opt Aut
0 12 1 11 0 0 1 1 0 0 1 0 0 0 0 0 0 0 0 0
! Ipr Ppl Ioc Mat Pcr Ls1 Ls2 Ls3 NLI Prf Ins Rpa Sym Hk1 Fou Sho Ana
0 2 1 1 1 0 0 0 0 -3 10 1 1 1 0 0 0 0
! Lambda1 Lambda2 Ratio Bkpos wdt Cthm muR AsyLim Rpolaz -> Patt# 1
1.541800 1.541800 1.0000 15.100 25.0000 0.0000 0.0000 35.00 0.0000
! NCY Eps R_at R_an R_pr R_gl Thmin Step Thmax PSD Sent0
2 0.30 0.50 0.50 0.50 0.50 20.3670 0.073338 60.0040 0.000 0.000
! 2Theta/TOF/E(kev) Background for Pattern# 1
22.009 10714.314 0.000
24.863 10714.314 0.000
27.954 10714.314 0.000
31.839 10714.314 0.000
36.040 13235.322 0.000
41.271 14495.808 0.000
46.899 13235.322 0.000
48.960 11974.799 0.000
52.765 13235.322 0.000
54.985 13235.322 0.000
59.661 11974.799 0.000
!
! 2 !Number of refined parameters
! Zero Code SyCos Code Sysin Code Lambda Code MORE -> Patt# 1
0.01257 21.00 0.00000 0.00 0.00000 0.00 0.000000 0.00 0
! Data for PHASE number: 1 ==> Current R_Bragg for Pattern# 1: 0.18
!-----
s102
!
! Nat Dis Ang Pr1 Pr2 Pr3 Jbt Irf Isy Str Furth ATZ Nvk Npr More
0 0 0 0.0 0.0 1.0 2 2 0 0 0 0 0.000 0 12 0
! -4 2 d <--Space group symbol
!-----> Profile Parameters for Pattern # 1

```

Figure 3.5: FULLPROF starting parameters file

The correct Bragg peak positions are identified and the respective cell parameters are yielded by the fit (Figure 3.5). Figure 3.6 shows an example of a Le Bail fit for data collected on RDP at 25°C . The red circles correspond to the data while the black line indicates the fit to the data. The green tick marks indicate the positions of the expected Bragg peaks, and the blue line is the difference between the data and the fit (which would be flat in the case of a perfect fit.)

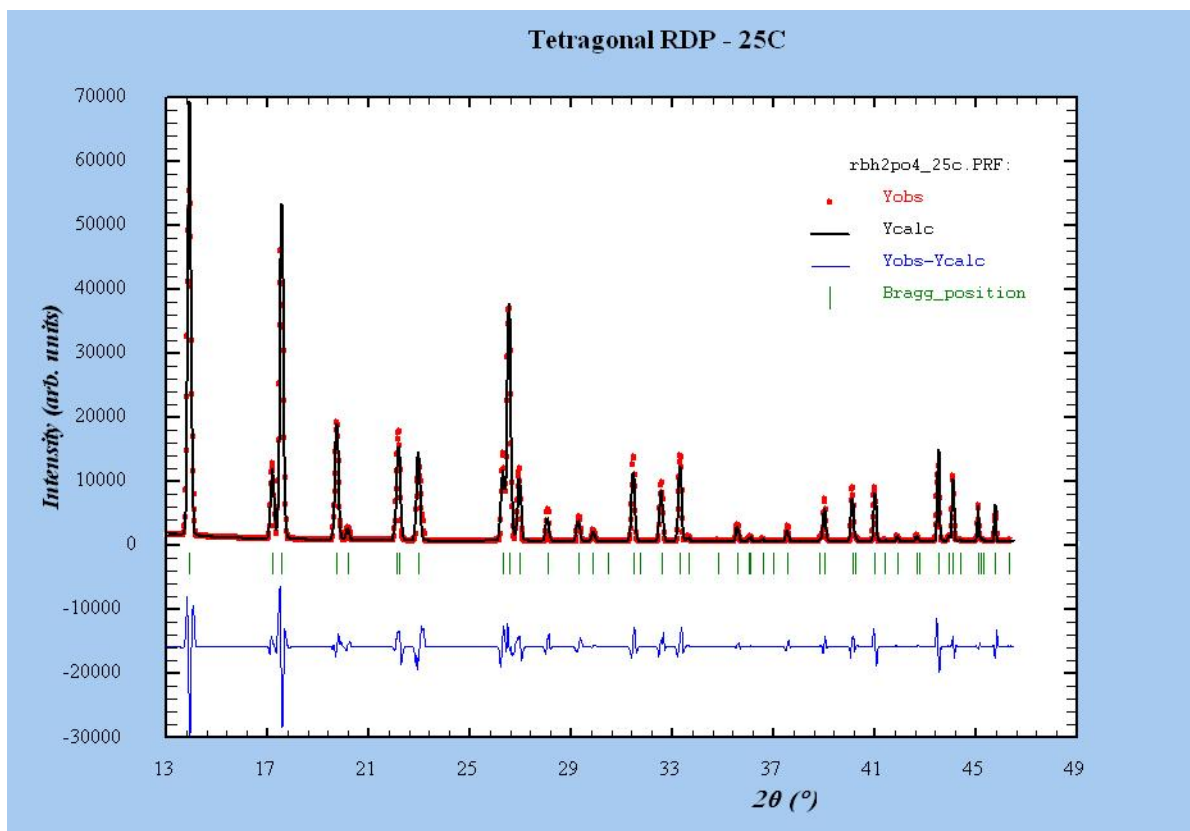
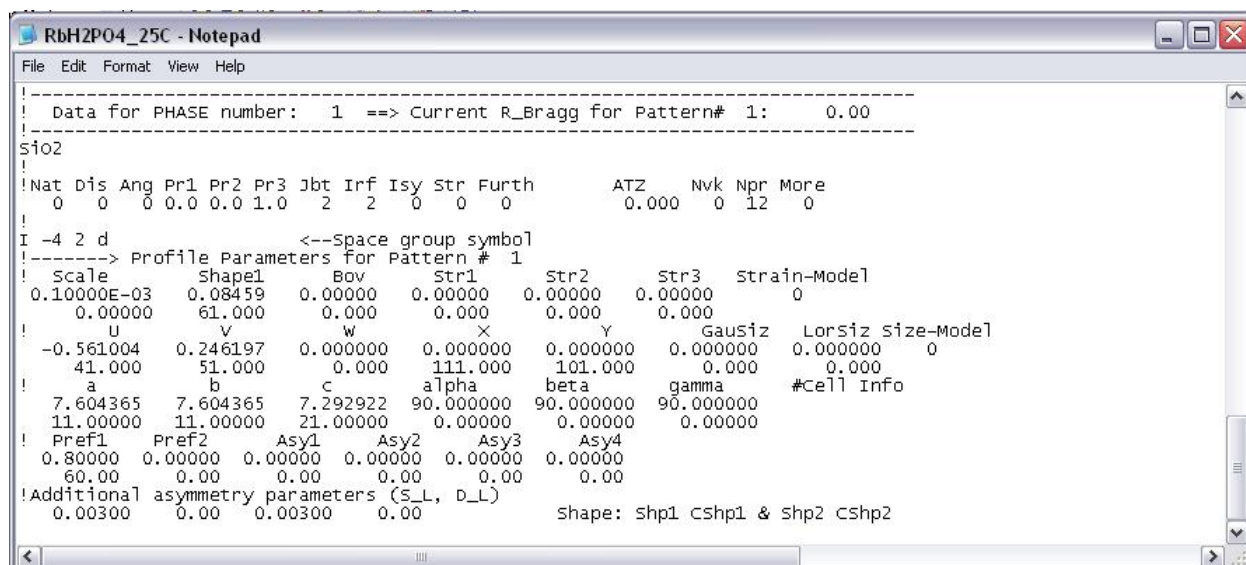


Figure 3.6: A Le Bail fit where red dots are XRD data points, black line is Le Bail fit and blue line is difference curve.



The second experiment consisted of powder diffraction measurements at temperatures ranging from approximately room temperature to 150°C. A Paar HTK high-temperature chamber was used in conjunction with the Siemens D500 diffractometer. The chamber raises the temperature of the sample by orders of the Job Measurement software. The chamber also protects the system from the high temperatures reached by the sample and sample holder, and permits the goniometer to work regularly at the same time.

Analysis on the diffraction patterns of RDP at high temperatures (30°C - 150°C) were performed using the FULLPROF software to get the lattice parameters from the best fit and consequently the crystal structure and lattice parameters identified.

Chapter 4: Results and discussion

Both phosphoric acids, RDP and CDP, have been shown to exhibit the so-called superprotonic behavior at elevated temperatures. In the case of CDP, the transition to the high-proton-conductivity state occurs at around $T=235^{\circ}\text{C}$. [25,26]. At room temperature, CDP has a monoclinic crystal structure. CDP then undergoes a phase transition to a cubic phase as the temperature rises to near $T=237^{\circ}\text{C}$ [15], a temperature commensurate with the onset of superprotonic behavior in the material. This has demonstrated that the monoclinic to cubic phase-transition in CDP is associated with its superprotonic behavior. On the other hand, RDP becomes superprotonic at a temperature of about $T=327^{\circ}\text{C}$ [8] but, unlike its phosphoric acid counter-part CDP, its room temperature phase is tetragonal, differing from the monoclinic room temperature state observed in CDP.

We found that polycrystalline RDP undergoes a phase transition when heated from room temperature to above 130°C . Figure 4.1 shows XRD patterns over the 20° - 60° 2θ range. According to the peak positions in Figure 4.1, only tetragonal RDP is present in the x-ray diffraction pattern when the heating went up to 80°C . Then, as the sample was heated above 90°C , the peaks of tetragonal RDP phase started to decrease in intensity, and new peaks started to emerge. A complete transformation was completed by 130°C when the peaks pertaining to tetragonal RDP completely disappeared. Further heating up to 200°C resulted in no further change in the XRD pattern.

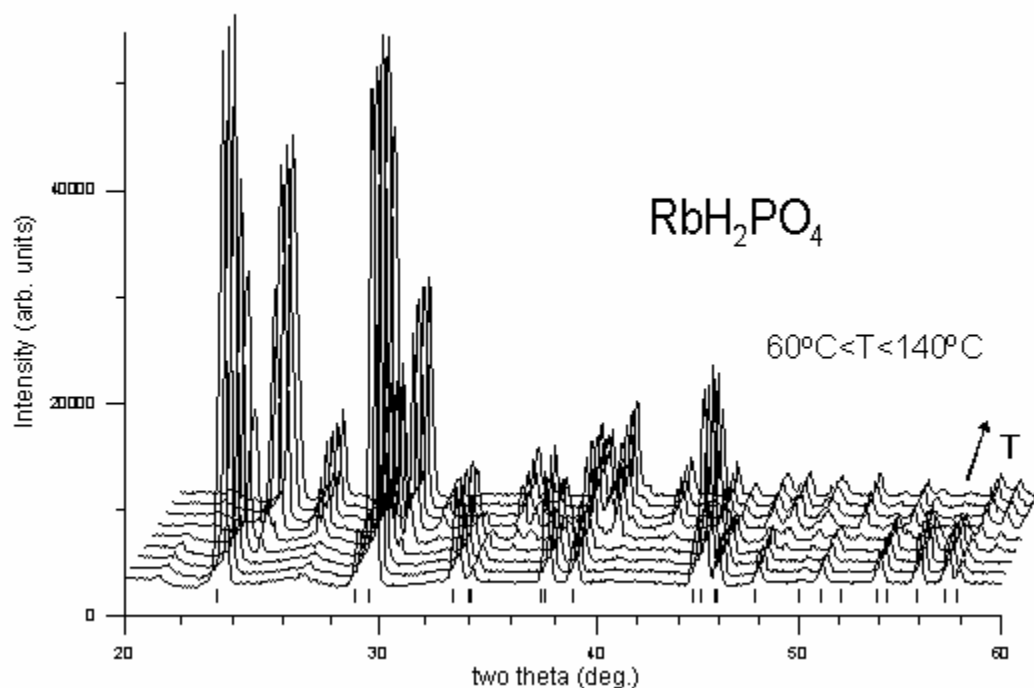


Figure 4.1: XRD pattern of RbH_2PO_4

Indexing was performed on the data collected at 150°C by means of a Le Bail fit using the program FULLPROF [27]. It was found that a single crystallographic phase with spacegroup $P2_1/m$ and unit cell parameters $a=7.694\text{\AA}$, $b=6.199\text{\AA}$, $c=4.774\text{\AA}$ and $\beta=109.02^\circ$ is present in the sample at this temperature (Figure 4.2 (b)). The starting unit cell parameters for the Le Bail fit of RDP at room temperature were taken from the Powder Diffraction File 84-0115; the unit cell parameters for the high-temperature phase were taken from the indexing of the 150°C data (Figure 4.2 (b)). Both fits were modeled by pseudo-Voigt functions. Thanks to the high-quality (low residue) in Figure 4.2, we were able to determine precisely the lattice parameters and to evidence clearly that tetragonal RDP transforms into a single monoclinic ($P2_1/m$) phase that is

stable at $T=150^{\circ}\text{C}$. This cleared the doubt of whether there would be a single phase or multiple phases present in the sample upon heating.

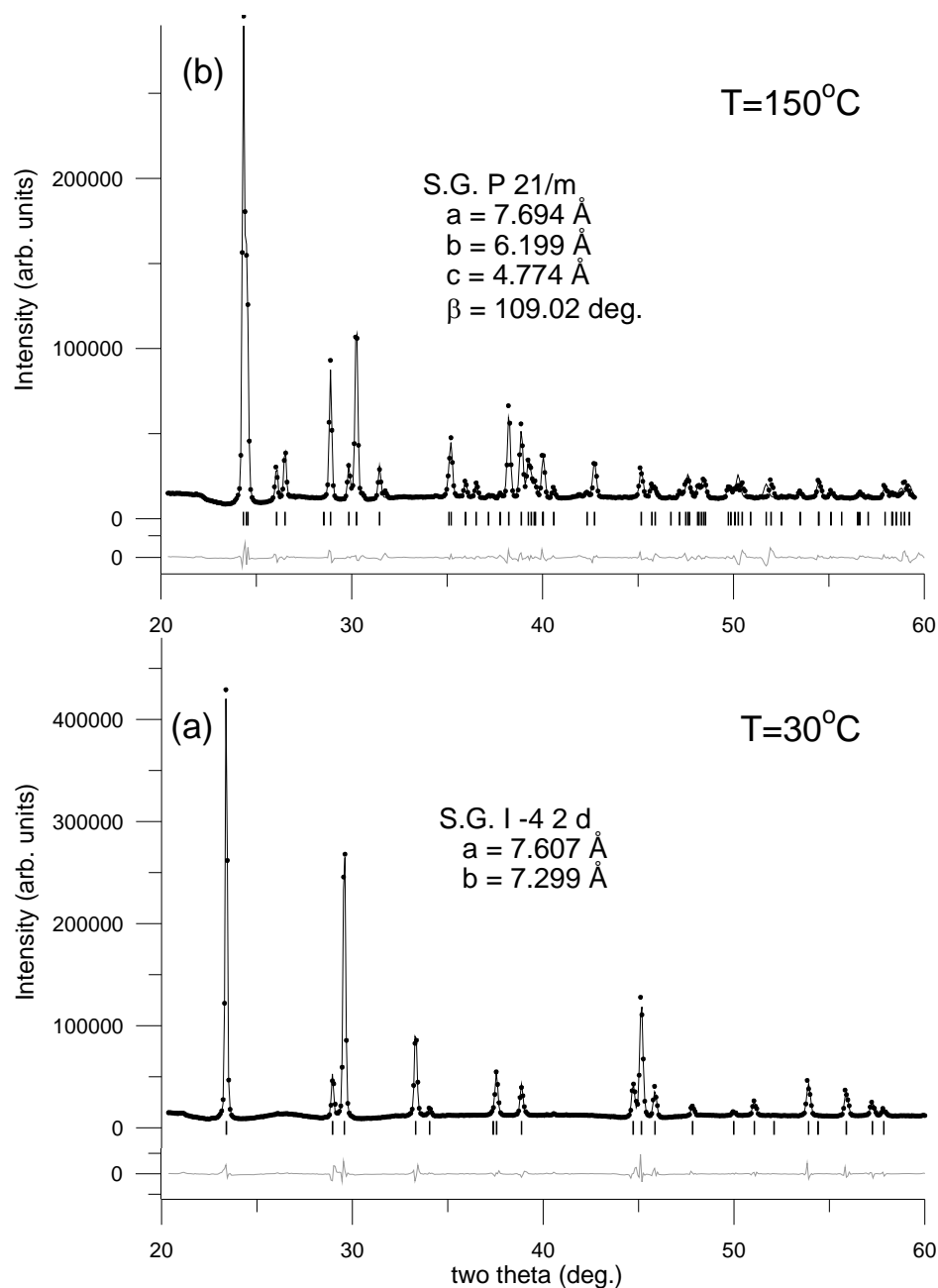


Figure 4.2: Indexing of RbH_2PO_4 at (a) room temperature: tetragonal RbH_2PO_4 . (b) high temperature: monoclinic RbH_2PO_4 .

After indexing the XRD pattern, a technique of analysis that is capable of determining, besides the unit cell dimensions, the atomic coordinates and the thermal parameters of the sample molecule was used. This method called Rietveld Refinement [28] uses the General Structure Analysis System (GSAS) [29] computer simulation program. A Rietveld refinement relates the peak shapes and positions with the cell parameters, atomic coordinates and internal energies of the atoms and makes the best fit possible between the observed profile and the refined profile. For the Rietveld refinement performed on RDP at $T=150^{\circ}\text{C}$, the lattice constants, space group, and peak-shape parameters yielded by the Le Bail analysis above were used as the starting parameters. In addition, the positions of the hydrogen atoms in monoclinic CDP ($P2_1/m$) were used as the starting positions for the hydrogen atoms in RDP at $T=150^{\circ}\text{C}$, assuming that both structures are isomorphic. Ultimately, a model of the RDP molecule in three dimensions was made (Figure 4.3). Soft constraints were imposed on the P-O bond distances and the O-P-O bond angles in the PO_4 tetrahedra 15 parameters were used in the Rietveld refinement and we got a final whole-pattern residual $R_{\text{wp}}=7.6\%$. Figure 4.3 shows the results of the Rietveld Refinement, where the solid line represents the best Rietveld fit, the empty symbols represent the actual intensities of the diffracted rays as a function of diffracted angles, the lower trace is the difference curve (between the observed and calculated patterns), and the vertical bars represent the position of the Bragg angles.

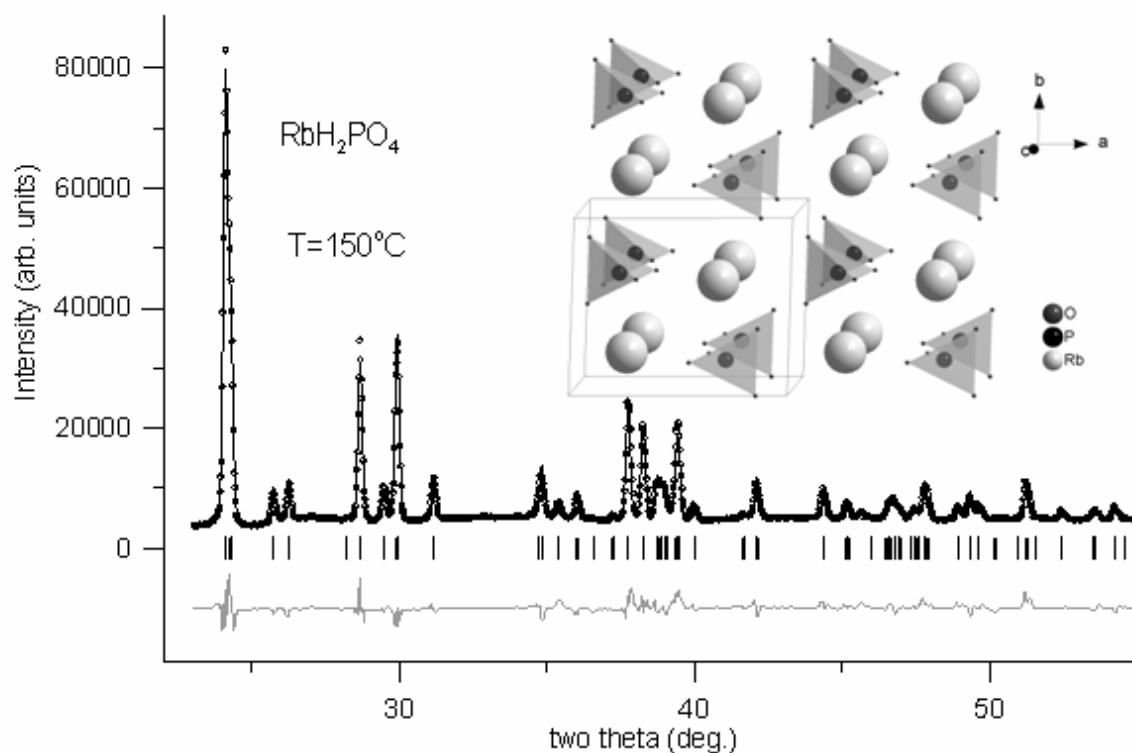


Figure 4.3: Rietveld fit and 3-D model of monoclinic RbH_2PO_4 .

The numerical results of the Rietveld refinement are shown in Table I, namely, the fractional coordinates of the non-hydrogen atoms and their thermal parameters. The resulting 3-D model of RbH_2PO_4 is shown in Figure 4.3. The 3-D model of the structure consists of alternating rows of PO_4 tetrahedra and Rb atoms that run parallel to the c axis. Each tetrahedron is hydrogen bonded at all four corners so that there are two types of hydrogen-bond chains zig-zagging along the a and c axes.

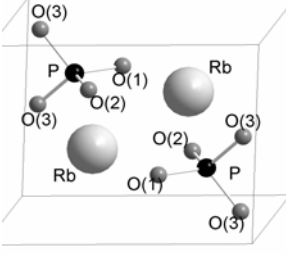
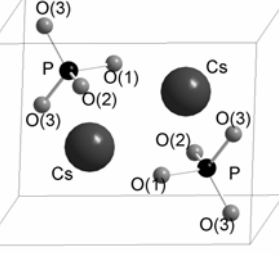
Table I: Fractional coordinates and thermal parameters of non-hydrogen atoms in RbH₂PO₄

Fractional coordinates and thermal parameters							
Atom	X	Y	Z	Multiplicity	Wyckoff letter	Occupancy	U _{iso}
Rb	0.2623(6)	0.25	0.0604(8)	2	E	1	0.0377(23)
P	0.2456(17)	0.75	0.5319(25)	2	E	1	0.0377(23)
O(1)	0.4156(26)	0.75	0.4132(33)	2	E	1	0.0377(23)
O(2)	0.3451(23)	0.75	0.8736(44)	2	E	1	0.0377(23)
O(3)	0.1289(35)	0.5482(51)	0.4203(42)	4	F	1	0.0377(23)

An important observation made through the Rietveld refinement was that the structure of monoclinic RDP is *nearly identical* to the structure from monoclinic CDP. Table II shows the parameters in a comparison between monoclinic RDP and CDP. Our finding that RDP transforms from a room temperature tetragonal phase into an intermediate temperature monoclinic phase, about 100°C below the superprotonic threshold (~257°C), suggests that RDP, like CDP, will transform into a high-symmetry disordered phase at a temperature close to the superprotonic threshold. In addition, this suggests that the nature behind the superprotonic conduction in both molecules, CDP and RDP, is fundamentally similar.

Further experiments were performed on RDP powders to investigate the stability of the newly found monoclinic phase of RDP at intermediate-to-high temperatures (above 150°C). In these experiments, we heated the RDP sample at temperatures from 30°C to 240°C in increments of 10°C using a synchrotron radiation source and a flat plate detector.

Table II. Comparison between unit cell parameters and PO₄ tetrahedral bond distances and angles in the monoclinic phases of rubidium- and cesium-dihydrogen phosphate.

	<i>RDP</i>	<i>CDP</i> [Ref. 7]
<i>Unit cell</i>		
Spacegroup	P 2 ₁ /m	P 2 ₁ /m
a [Å]	7.868(6)	7.912(2)
b [Å]	6.299(5)	6.383(1)
c [Å]	4.871(4)	4.8802(8)
β [deg.]	109.15(3)	107.73(2)
<i>Phosphate group tetrahedral bond distances and angles</i>		
P-O(1) [Å]	1.622(19)	1.565(6)
P-O(2) [Å]	1.590(18)	1.481(5)
P-O(3) [Å]	1.558(7)	1.529(4)
O(1)-P-O(2) [deg.]	101.1(9)	107.0(3)
O(1)-P-O(3) [deg.]	109.6(6)	106.1(2)
O(2)-P-O(3) [deg.]	113.4(6)	113.6(2)
O(3)-P-O(3) [deg.]	109.4(7)	109.9(2)

XRD data was collected in intervals of about 45 s. Full profile analysis using Le Bail fits were performed on the patterns acquired at each temperature. On the upper row of Figure 4.4, Le Bail fits of the patterns at three different temperatures within the intervals (30°C – 90°C, 90°C – 130°C, and 130°C – 200°C) are shown. In the 30°C – 90°C interval (region I), only the tetragonal phase of RDP is present; in the 90°C – 130°C interval (region II), both the tetragonal

and the monoclinic phases are present; and in the 130°C – 200°C interval (region III), only monoclinic RDP is present.

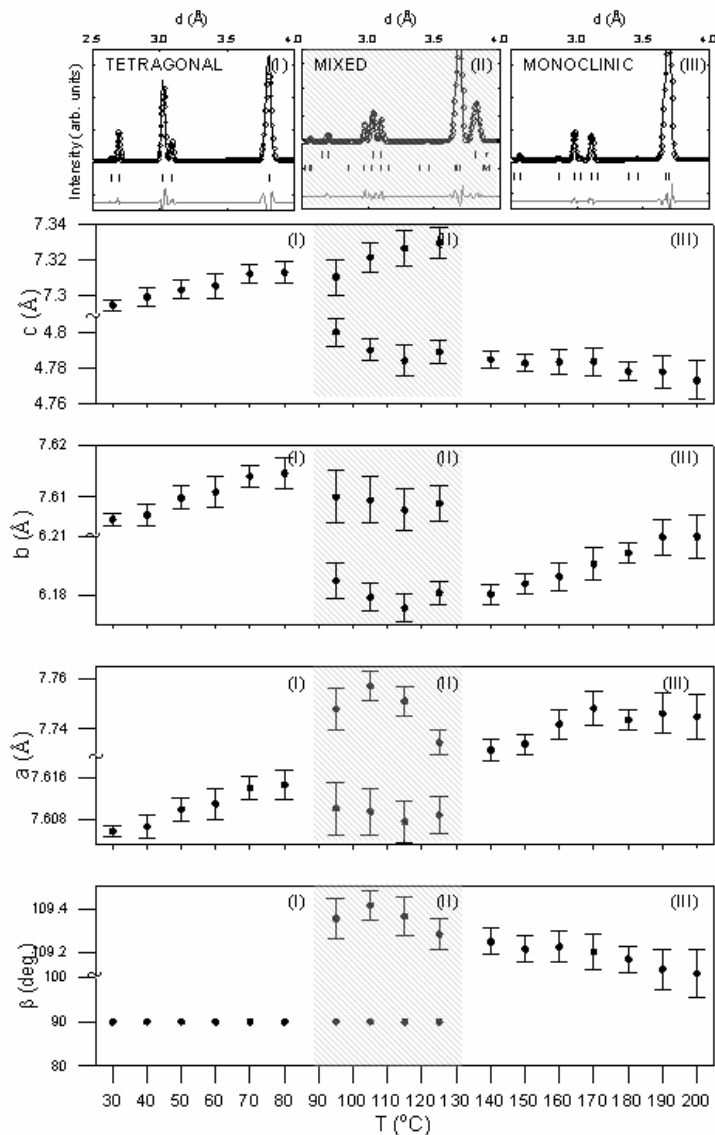


Figure 4.4: Le Bail fits for three regions (upper panel) . Temperature dependence of lattice parameters of RbH_2PO_4 .

In the lower panels of Figure 4.4, the temperature dependence of the lattice parameters of both tetragonal and monoclinic RDP obtained from the Le Bail fits are shown. With the exception of the clearly different pattern of lattice parameters for each RDP phase, this observed

temperature dependence demonstrates a smooth variation of the lattice parameters throughout the whole 30°C – 200°C temperature interval, showing that no other structural or chemical modifications (except for the tetragonal→monoclinic polymorphic transition) occur. These results confirm that monoclinic RDP is stable when heated up to 200°C. Many authors have indicated that the tetragonal to monoclinic transition occurs at a particular temperature in the 80°C – 120°C interval, depending on the sample and experimental conditions [30]. Our results show that because both phases of RDP (tetragonal and monoclinic) coexist in the 90°C – 130°C interval, the phase transition is gradual and a precise temperature at which the transition occurs could not be determined. A final XRD experiment on polycrystalline RDP was performed to investigate its behavior at high temperatures (above 200°C) and at ambient pressure and humidity conditions. Figure 4.5 shows XRD patterns collected at five different temperatures in the 200°C – 240°C interval.

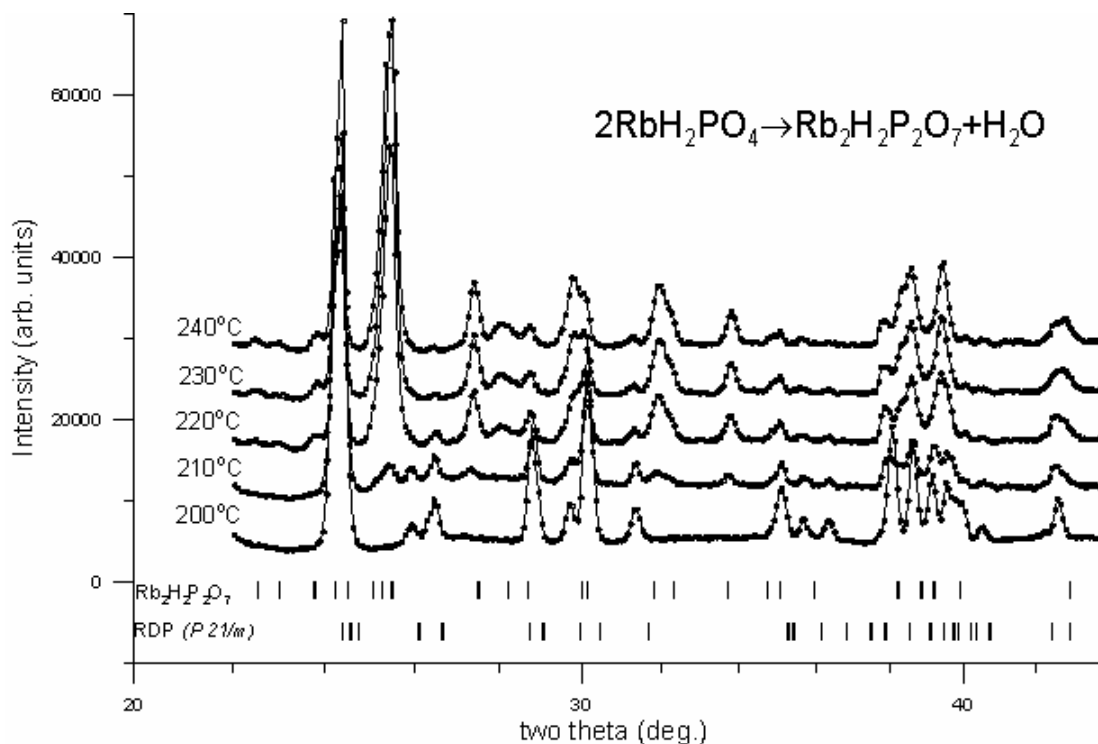


Figure 4.5: Dehydration and partial decomposition of RbH_2PO_4 at high temperatures.

From these patterns we were able to observe new peaks emerging at even higher temperatures. The new peaks were indexed and corresponded to the material di-rubidium di-hydrogen pyrophosphate ($\text{Rb}_2\text{H}_2\text{P}_2\text{O}_7$). These new peaks emerge as the result of dehydration and partial polymerization/decomposition of the sample via the reaction $2\text{RbH}_2\text{PO}_4 \rightarrow \text{Rb}_2\text{H}_2\text{P}_2\text{O}_7 + \text{H}_2\text{O}$. At 240°C , the new peaks are dominant, but the monoclinic RDP peaks are still present in the XRD pattern. In comparison, CDP starts to dehydrate/decompose at almost the same temperature as it jumps into a superprotonic behavior. Moreover, the phase transition in CDP from monoclinic to cubic, to which its superprotonic behavior is associated, was seen even in an ambient atmosphere [15]. Unfortunately, the partial decomposition of RDP, which starts at about $T=210^\circ\text{C}$, occurs at more than one hundred degrees Celsius below the temperature at which RDP was observed to become superprotonic ($T=327^\circ\text{C}$) [8]. This partial decomposition of RDP is the reason why a potential phase transition to a superprotonic RDP transition cannot be observed under ambient pressure. Therefore, in order to investigate if the superprotonic behavior is indeed due to a polymorphic phase transition from a monoclinic to a high-temperature superprotonic phase, experiments under a high pressure or saturated water vapor environment are needed.

Chapter 5: Summary and conclusions

We performed XRD experiments on polycrystalline RDP samples by heating the samples from room temperature to $T=250^{\circ}\text{C}$ using laboratory and synchrotron x-ray sources under ambient pressures. We observed that RDP undergoes a polymorphic phase transition from its room-temperature crystal structure to an intermediate-temperature monoclinic structure. The transition starts at about $T=90^{\circ}\text{C}$ and is complete at about $T=130^{\circ}\text{C}$. Both, the tetragonal and the monoclinic phases are present in the transition-temperature interval. The new, intermediate-temperature, monoclinic RDP phase crystallizes in spacegroup $P2_1/m$ with unit cell parameters $a=7.694\text{\AA}$, $b=6.199\text{\AA}$, $c=4.774\text{\AA}$ and $\beta=109.02$ deg. Monoclinic RDP is nearly identical in structure to monoclinic CDP. This means that it is expected that similar structural transitions and similar proton conduction mechanisms in both of these phosphate-based solid acids are responsible for their superprotonic behavior. Upon further heating under ambient pressure and humidity conditions, the monoclinic RDP polymorph is stable up to 200°C . After this temperature, RDP starts to dehydrate/decompose into water and rubidium di-hydrogen pyrophosphate salt via the reaction reaction: $2\text{RbH}_2\text{PO}_4 \rightarrow \text{Rb}_2\text{H}_2\text{P}_2\text{O}_7 + \text{H}_2\text{O}$. Experiments under high pressure or saturated water vapor environment are needed in order observe a high-temperature phase transition that might be associated to the superprotonic behavior of RDP.

References

- [1] Larminie and A. Dicks, Fuel Cell Systems Explained. (2000).
- [2] B. Winther-Jensen, O. Winther-Jensen, M. Forsyth and D. R. MacFarlane, Science 321 (1159267) (2008).
- [3] R. Eckl, W. Zehner, C. Leub and U. Wagner, Journal of Power Sources 138 (1-2) (2004).
- [4] Baranov et al., JETP Lett 36, 459 (1982).
- [5] Haile et al., Nature 410, 410 (2001).
- [6] R. B. Merle, C. R. I. Chisholm, D. A. Boysen and S. M. Haile, Energy and Fuels 17, 210-215 (2003).
- [7] D.A. Boysen, S.M. Haile, H. Liu, and R.A. Secco, Chem. Mater. **15**, 727(2003).
- [8] D.A. Boysen, S.M. Haile, H. Liu, and R.A. Secco, Chem. Mater. **16**, 693(2004).
- [9] D.A. Boysen, T. Uda, C.R.I. Chisholm, and S.M. Haile, Science, **303**, 68(2004).
- [10] N. M. Plakida, Phys. Status Solidi B, **135**, 133(1986).
- [11] K.-S. Lee, J. Phys. Chem. Solids 57 (3) (1996).
- [12] E. Ortiz, E. A. Vargas, G. Cuervo, B.-E. Mellander, and J. Gustafson, J. Phys. Chem. Solids **59**, 1111(1998).
- [13] E. Ortiz, R. A. Vargas and B.-E. Mellander, Journal of Chemical Physics 110 (10) (1999).
- [14] J.-H. Park, Phys. Rev. B **69**, 054104(2004).
- [15] C. E. Botez, J. D. Hermosillo, J. Zhang, J. Qian, Y. Zhao, J. Majzlan, R. R. Chianelli, and C. Pantea, J. Chem. Phys. **127**, 194701(2007).
- [16] W. Bronowska, J. Chem. Phys. **114**, 611(2001).

- [17] A.I. Baranov, V.P. Khiznichenko, and L.A. Shuvalov, *Ferroelectrics* **100**, 135(1989).
- [18] A. Ishikawa, H. Maekawa, T. Yamamura, Y. Kawakita, K. Shibata, and M. Kawai, *Solid State Ionics* **179**, 2345(2008).
- [19] R. Blinc, J. R. Ferraro, and C. Postmus, *J. Chem. Phys.* **51**, 732(1969).
- [20] J.-H. Park, K.-S. Lee, and J.-N. Kim, *J. Phys.: Condens. Matter* **10**, 9593(1998).
- [21] J.-H. Park, K.-S. Lee, and B.-C. Choi, *J. Phys.: Condens. Matter* **13**, 9411(2001).
- [22] W. L. Bragg, *Proc. R. Soc. London, Ser. A.* **89**, 248–291(1913).
- [23] C. Kittel, *Introduction to Solid State Physics*, Third Edition ed. (John Wiley and Sons, Inc., New York, 1968).
- [24] J. D. Patterson and B. C. Bailey, *Solid-State Physics*. (Springer, Berlin, 2007).
- [25] S. M. Haile, *MRS Symposia Proceedings No. 547*, (Materials Research Society, Pittsburg, 1999), p. 315.
- [26] A.I. Baranov, V.P. Khiznichenko, and L.A. Shuvalov, *Ferroelectrics* **100**, 135(1989).
- [27] J. Rodriguez-Carvajal, *Abstracts of the Powder Diffraction Meeting, Toulouse, France*, pp. 127-128 (1990). Program and documentation available from <http://www-llb.cea.fr/fullweb/fullprof.htm>.
- [28] H. M. Rietveld, *J. Appl. Crystallogr.* **2**, 65(1969).
- [29] A. C. Larson and R. B. Von Dreele, *Los Alamos National Laboratory Report No. LA-UR-86-784*, Los Alamos, (1987). Program and documentation available from <http://public.lanl.gov/gsas>.
- [30] B. Metcalfe, J. B. Clark, *Thermochim. Acta* **24**, 149(1978).

Curriculum Vita

Heber Martinez was born in Ciudad Juarez, Chihuahua Mexico. The fourth child of Manuel Martinez and Eva Salinas, he graduated from Preparatoria Federal por Cooperacion “El Chamizal”, in the spring of 2001 and entered The University of Texas at El Paso in the fall. He graduated from UTEP with a B. S. in Physics in the spring of 2006. He entered the Masters in Physics program at UTEP in the summer of 2006. He is co-author of the article *High-temperature crystal structures and chemical modifications in RbH_2PO_4* . He has been a Teaching Assistant since the spring of 2007 for Astronomy Laboratory, General Physics I Laboratory (Non-calculus based introductory mechanics), and General Physics II Laboratory (Non-calculus based electricity and magnetism).

Permanent address: 6332 Calle Pino
El Paso, TX 79912

This thesis was typed by Heber Martinez.